HHS Public Access

Author manuscript

ACS Nano. Author manuscript; available in PMC 2023 August 28.

Published in final edited form as:

ACS Nano. 2023 April 25; 17(8): 7797–7805. doi:10.1021/acsnano.3c00638.

Enhanced Nanobubble Formation: Gold Nanoparticle Conjugation to Qβ Virus-Like Particles

Perouza Parsamian[a], **Yaning Liu**[b], **Chen Xie**[b], **Zhuo Chen**[a], **Peiyuan Kang**[b], **Yalini H. Wijesundara**[a], **Noora M. Al-Kharji**[a], **Ryanne Nicole Ehrman**[a], **Orikeda Trashi**[a], **Jaona Harifidy Randrianalisoa**[c], **Xiangyu Zhu**[d], **Matthew D'Souza**[a], **Lucas Anderson Wilson**[a], **Moon J. Kim**[d], **Zhenpeng Qin**[b], **Jeremiah J. Gassensmith**[a,e]

[a]Department of Chemistry and Biochemistry University of Texas at Dallas 800 West Campbell Road, Richardson, Texas 75080-3021, United States

[b]Department of Mechanical Engineering University of Texas at Dallas 800 West Campbell Road, Richardson, Texas 75080-3021, United States

[c]Institut de Thermique, Mécanique, Matériaux – ITheMM EA 7548 Université de Reims Champagne-Ardenne, Campus Moulin de la Housse, F-51687, Reims, France

[d]Department of Materials Science and Engineering University of Texas at Dallas 800 West Campbell Road, Richardson, Texas 75080-3021, United States

[e]Department of Biomedical Engineering University of Texas at Dallas 800 West Campbell Road, Richardson, Texas 75080-3021, United States

Abstract

Plasmonic gold nanostructures are a prevalent tool in modern hypersensitive analytical techniques such as photoablation, bioimaging, and biosensing. Recent studies have shown that gold nanostructures generate transient nanobubbles through localized heating and have been found in various biomedical applications. However, the current method of plasmonic nanoparticle cavitation events has several disadvantages, specifically including small metal nanostructures (≤10 nm) which lack size control, tuneability, and tissue localization by use of ultra-short pulses (ns, ps) and high-energy lasers which can result in tissue and cellular damage. This research investigates a method to immobilize sub-10 nm AuNPs (3.5 and 5 nm) onto a chemically modified thiol-rich surface of Qβ virus-like particles (VLPs). The findings demonstrated that the multivalent display of sub-10 nm gold nanoparticles causes a profound and disproportionate increase in photo-cavitation by upwards of five-to-seven-fold and significantly lowered the laser fluency by

CORRESPONDING AUTHORS: Zhenpeng Qin — Department of Mechanical Engineering, The University of Texas at Dallas, Richardson, Texas 75080, United States, Zhenpeng.Qin@utdallas.edu; Jeremiah J. Gassensmith — Department of Chemistry and Biochemistry and Department of Biomedical Engineering, The University of Texas at Dallas, Richardson, Texas 75080, United States, Gassensmith@utdallas.edu.

AUTHOR CONTRIBUTIONS

Primary manuscript writing was done by P.P, Z.C, J.J.G, Y.L, C.X, and Z.Q. AuNP synthesis, bioconjugation, QβSH, and QβAuNP characterization were done by Z.C. and P.P. TEM micrographs were collected by Y.W. STEM micrographs were done by X.Z and M.K, Qβ synthesis was done by P.P, N.A, R.N.E, O.T, M.B.D, L.A.W. Nanobubble studies was done by Y.L and K.P. Nano-thermal transport computational studies were performed by Y.L, C.X, and J.R.

Supporting Information

The Supporting Information is available free of charge at…SI showing materials and methods, additional characterization, and figures.

four-fold when compared to individual sub-10 nm gold nanoparticles. Furthermore, computational modeling showed that the cooling time of QβAuNP scaffolds is significantly extended than that of individual AuNPs, proving greater control of laser fluency and nanobubble generation as seen in the experimental data. Ultimately, these findings showed how QβAuNP composites are more effective at nanobubble generation than current methods of plasmonic nanoparticle cavitation.

Keywords

plasmonic; gold nanoparticles; virus-like particles; plasmonic nanobubble; transient heating

Introduction:

Plasmonic gold nanostructures are among the most well-known and oldest nanotechnologies and can be found in applications from modern hypersensitive analytical techniques to ancient art[1]. The contemporary utility of gold nanostructures is owed to their straightforward synthesis and tunable intense color, which arises from a photo-induced oscillation of surface electrons creating the plasmon.[2–5] These plasmonic nanostructures can be designed to efficiently convert incident laser energy into heat, known as the photothermal effect, and have found wide applications in photothermal therapies and point-of-care diagnostics.[6–8] One of the potential responses to the photothermal effect is nanobubble generation. By tuning the topology of the nanostructure and the heating duration, transient nanobubble cavitation and collapse can be observed, which creates significant shear forces capable of temporarily or permanently altering vasculature.[9–11]

These sheer forces, which arise from the rapid cavitation of the nanobubble, are powerful enough to remodel tissue. This has given them utility in nano-surgical applications; for instance, recent work has found that plasmonically induced cavitation events can create temporary openings in the blood-brain barrier.[12, 13] With state-of-the-art methodologies using small metal nanostructures (< 10 nm), effective methods of plasmonic nanostructure cavitation lack size control, tuneability, and tissue localization.[14–19] An articulated drawback to utilizing these metal nanostructures is that they require ultra-short pulsed lasers and high laser energy, which can induce unwanted tissue damage.[20–27] Thus, finding new architectures and composites of gold that can reduce the laser flux can help spare healthy tissue and reduce the amount of gold needed for a therapeutic effect. This cavitation effect has been enhanced upon aggregation of gold nanoparticles, albeit with larger nanoparticles. For instance, intracellular clustering of AuNPs has been shown to induce greater vapor nanobubble generation, enabling mechanical disruptions of the cell membrane via direct AuNP therapies.[28] Other studies also combined chemotherapy with plasmonic nanobubbles to achieve efficient thermal destruction of cancer cells by taking advantage of the formation of NP clusters, showing promise for *in-vivo* nanoparticle-based photothermal therapies.[22, 24, 29]

Herein, we show the colocalization of many sub-10-nm AuNPs via immobilization onto a virus-like-particle (VLP) as a superior alternative to individual sub-10 nm AuNPs (Scheme 1). Virus-like particles (VLPs) are non-infectious engineered biodegradable nanostructures

derived from viral proteins. The structure of most VLPs is known to atomistic detail, and their exposed surfaces can be functionalized using high-yielding bioconjugation chemistry. In particular, VLP Qβ—the crystal structure displayed in Figure 1A—has been used extensively as a proteinaceous nanocarrier, as its well-understood surface chemistry, minimal toxicity, and low reactogenicity have made it an ideal biodegradable delivery platform.[30] Qβ is an icosahedral VLP comprised of 180 coat proteins connected through disulfide bonds (Figure 1A yellow residues) with four solvent-exposed primary amine residues from lysine (Figure 1A green residues), which have been chemically modified for use in multiple biomedical applications, including contrast agents, photothermal scaffolds, and drug carriers.[31–48]

In this work, we detail a method to immobilize either 3.5 or 5 nm AuNPs onto a chemically modified thiol-rich surface of Qβ. We found that the multivalent display of approximately 46 sub-10 nm gold nanoparticles (AuNPs) induces a significant increase in the photo-cavitation efficiency by five-fold compared to traditional sub-10 nm gold nanoparticles. Computational modeling shows that the absorption cross-section (C_{abs}) for the QβAuNP conjugation is higher than that of the single AuNP heating due to the plasmonic coupling. Notably, the heating overlap leads to a significantly higher maximum temperature rise in water and longer cooling time versus single AuNP heating, which may account for the increased nanobubble signal.[49] The plasmonic and heat coupling contributes to the significant increase in photo-cavitation efficiency.

Results and Discussion:

The synthesis of the polyvalent VLP-gold nanosystem began with the functionalization of the solvent-exposed amine residues of Qβ with 3-mercaptopropionic acid (MPA). MPA was conjugated in a single set via EDC/sulfo-NHS coupling under mildly acidic conditions to yield the thiolated VLP QβSH (Figure 1B). The successful thiolation of Qβ was determined by electrophoretic mobility assays, and the retention of the spherical morphology was confirmed through Dynamic Light Scattering (DLS) and Transmission Electron Microscopy (TEM). As depicted in Figure 1C, DLS showed almost no change in hydrodynamic radius between Qβ (Z-average: 31.09 ± 1.00 d. nm) and the thiolated Qβ (QβSH) (Z average: 31.49 ± 0.27 d. nm). As expected, TEM micrographs confirmed no changes to the size or morphology between Qβ (Figure 1D) and QβSH (Figure 1E). Conjugation was confirmed by electrophoretic mobility through 1% agarose gel (Figure 1F), which showed a significant shift for QβSH toward the positive electrode. This shift is anticipated as a result of converting the positively charged lysines into thiol-terminated amides. The colorimetric thiol-selective Ellman's assay was used to quantify free thiols and revealed that approximately 189 ± 0.0106 thiols were conjugated onto the surface of Qβ. Lastly, SDS-**PAGE** (Figure 1G) shows monomer (14.5 kDa) and dimer coat proteins running approximately the same distance, which is anticipated based on the very low M.W. (106 Da) of the MPA. From these results, we conclude that QβSH remains intact and possesses approximately one free thiol per coat protein.

Following successful bioconjugation to create a thiol-rich Qβ, we turned to immobilize AuNPs onto the viral surface.

We chose to use 3.5 and 5 nm AuNPs, to study differences in their ability to attach to the surface of QβSH and assess the photothermal responses of two variably-sized plasmonic AuNPs. Attachment of AuNPs to Qβ was done in MilliQ Ultrapure water at a pH of 7 at room temperature (rt) for 12–15 h Figure 2A. As shown in Figure 2B, dynamic light scattering (DLS) shows an expected increase in hydrodynamic radius. Both composites 3.5 nm (Z-average 40.03 ± 0.17 d. nm) and 5 nm (Z average: 67.48 ± 4.69 d. nm) exhibit an increase in size, with the larger 5 nm gold creating a larger composite nanoparticle. These size distributions of the QβAuNP composites were assessed by scanning transmission electron microscopy (STEM High-Angle Annular Dark Field imaging (HAADF), and the results are shown in Figure 2C.

To further understand how much gold was attached to each virus, we investigated the number of AuNP immobilized onto Qβ. A histogram was produced from visual analysis of STEM micrographs, and individual AuNPs were counted on QβSH VLPs. Each scaffold showed an average of 46 individual AuNPs per surface-functionalized QβSH (Figure 2D) (n=32). The apparent difference in distribution is likely a result of experimental variation. STEM imaging allows us to visualize the boundaries of overlapping gold nanostructures, which helps make it clear that the AuNPs are evenly distributed on the surface of the VLP and have not aggregated nor changed diameter. Widefield imaging (Figure S2H) with TEM shows little to no unconjugated gold nanoparticles in solution, agreeing with our electrophoretic mobility assay. Interestingly, UV-Vis spectroscopic analysis shows a significant redshift of the free AuNPs when bound to Qβ (Figure 2E). Since the gold nanoparticle diameters are unchanged per STEM imaging, we suspect this shift results from the plasmonic coupling between close AuNPs. When attached to the virus, the smaller gold nanostructures have a slightly larger bathochromic shift (9 nm vs. 7 nm). Electrophoretic analysis on 1% agarose shows no free Qβ or QβSH, which suggests that all the QβSH has been functionalized with AuNPs (Figure 2F).

Nanobubble generation and detection

Next, we investigated the photothermal effects of conjugated QβAuNP complex versus free AuNPs, by activating and detecting the plasmonic nanobubble (PNB). PNBs are formed when the pulsed pump laser beam activates the AuNP-based samples flowing through the microscale detection zone. The confined heating within this zone causes localized evaporation of the media surrounding the AuNPs, creating the PNBs. The resulting PNBs optically scatter light and can be synchronically detected by a continuous probe laser (Figure 3A). Since the PNBs are transient events with sub-microsecond lifetimes, we set the pump laser with a repetition rate of 50 Hz and sample flow speed of 10 μL/min, avoiding repeated heating and detection of the same PNB event. Inside a microcapillary (Figure 3B), two colocalized laser beams — a probe laser beam (Figure 3C) and a pump laser beam (Figure 3D) — are aligned together (Figure 3E) to create a virtual detection zone. We first tested individual AuNPs and QβAuNPs of different sizes at a high laser fluence (29.3 mJ/cm^2) to observe PNB signals for all samples. In particular, we tested 3.5 nm AuNPs (Au3.5), Qβ with 3.5 nm AuNPs attached to the surface (QβAu3.5), 5 nm AuNPs (Au5), and Qβ with 5 nm AuNPs attached to the surface (QβAu5). All samples were prepared at the same optical densities (O.D. = 0.4), ensuring equivalent optical absorption for PNB testing. Among those

tested samples (Figure 3F), both QβAu3.5 and QβAu5 conjugates result in increased signals corresponding to the larger PNBs generated as compared to free particles— Au3.5 and Au5, respectively. On the other hand, when we slightly alter the size of AuNPs on Qβ (*i.e.*, from 3.5 to 5 nm), QβAu5 further enhances PNB signals dramatically. To fully investigate their thermal responses, we examined the PNB generation for each case under various laser fluences. Figure 3G depicts representative PNB signal traces (10 pulses) collected for Au3.5, QβAu3.5, Au5, and QβAu5, respectively, and shows laser energy-dependent PNB signals.[50] At no laser or low laser fluence condition, no PNB signal was detected, whereas higher laser fluence leads to larger PNB signals. Compared with small Au3.5 and Au5, large Au aggregates (*i.e.*, QβAu3.5 and QβAu5) tend to produce PNBs much easier. To understand this phenomenon, we analyzed the PNB signals by their unique amplitudes (Figure 3H), lifetimes (Figure 3I), and generation threshold (Figure 3J). We found linear correlations between the amplitude and lifetime of PNB signals versus the laser fluence for all the tested samples. We compared the slopes of the amplitude and lifetime plots for Au3.5, Au5, QβAu3.5, and QβAu5. Notably, QβAu3.5 and QβAu5 conjugates have slopes of amplitudes that are 7.7- and 5.7- times higher than the Au3.5 and Au5, respectively. Similar trends are exhibited in the lifetime plot, where QβAu3.5 and QβAu5 conjugates have slopes that are 4.8- and 4.4- times higher than the Au3.5 and Au5, respectively. QβAu5 impressively doubled the slope of QβAu3.5, indicating its long bubble-breaking time because of the larger bubble size. Lastly, we explored the PNB generation threshold for each sample (Figure S3). Here the PNB generation threshold (F_{thresh}) was defined at the laser fluence with 50% PNB probability, which describes the minimal amount of laser fluence required to expand the vapor bubble around AuNPs. In the probability plot, Au3.5 and Au5 require high laser fluence to create the PNBs (F_{thresh} = 34.7 and 8.5 mJ/cm^2). QβAu3.5, considered a cluster of Au3.5, dramatically lowered the PNBs threshold to 4.5 mJ/cm^2. Furthermore, increasing the size of AuNP conjugated onto Qβ lowers the PNB generation threshold, thus tuning the thermal responses. For example, QβAu5 possesses a mild PNB generation threshold of 0.45 mJ/cm^2, which opens possibilities for non-invasive *in-vivo* studies using laser treatment while maintaining tissue integrity.[51, 52] Together, QβAu5 exhibits superior thermal responses over all tested samples owing to its highest PNB amplitude, lifetime, and lowest PNB generation threshold.

Nano thermal transport of conjugated QβAuNPs

Lastly, we investigated the plasmonic and heat coupling of QβAuNPs by numerical simulations. We first determined the plasmonic and heating response for the QβAuNPs composites with a 3D-FEM simulation model (Figure 4A). Figure 4B–E shows the near filed enhancement ($(E/E_0)^2$) profile with λ = 532 nm and temperature rise (ΔT) profiles (t = 26 ps, 35 ps) for QβAuNP conjugation and free AuNP, respectively. As illustrated in the $(E/E_0)^2$ profiles, for both QβAu5 and QβAu3.5, the plasmonic coupling is minimal and can only lead to a slight increase in the absorption cross-section (C_{abs}) compared with that of the single AuNP (Figure 4F and Table S1). In contrast, as shown in Figure 4B–E, despite limited heating overlap at the end of the laser pulse (t_1 = 26 ps), further heat dissipation after the laser pulse (t_2 = 35 ps) leads to significant heating overlap, leading to collective heating between the AuNPs. We further analyzed this heating process with the temporal evolution of ΔT at representative locations. Figure S4 shows that, under laser radiation (34.8 mJ/cm^2),

the temperature rise in AuNP (ΔT_1) increases rapidly to 1375 K for QβAu5 and 794 K for QβAu3.5. After the laser pulse, the AuNP cools gradually while the heat dissipates into the water domain and leads to heating overlap between AuNPs,[53] which is evidenced by an increasing temperature rise at the mid-point among AuNPs (ΔT_2). After the ΔT_2 reaches its peak value, it starts to cool down with further dissipation. Next, we compared the maximum of ΔT_1 and ΔT_2 for QβAuNPs and AuNP, respectively (Figure 4G–H). The maximum ΔT_1 for QβAuNP conjugation and free AuNP are similar, whereas the maximum for ΔT_2 for QβAuNP conjugation is significantly higher than that of free AuNP. Moreover, smaller AuNPs have a higher surface-volume ratio that can enhance heat dissipation and cooling. Importantly, for the same-sized AuNP, ΔT_2 for QβAuNPs conjugation is significantly higher than that of the single AuNP. This could be via the heating overlap between AuNPs in the conjugation, leading to a longer cooling time (Figure 4G). It should be noted that the mechanism of the nanobubble generation under the nanoscale is still unclear. Considering all these factors, the difference in the geometries of QβAuNPs and single AuNP, the size dependence of heating, the heating overlap at the mid-points between AuNPs, and a longer cooling time may all facilitate the nanobubble generation and lowered energy threshold for nanobubble detection with QβAuNP5 (Figure 3J).

Conclusion:

In summary, immobilizing multiple size-controlled sub-10nm AuNPs onto chemically modified thiol-rich virus-like particles provides a superior alternative to current state-of-the-art methodologies for plasmonically induced cavitation events. In this work, we exposed our scaffolds to high laser fluencies to elucidate the generation of plasmonic nanobubbles (PNBs) and compared their photothermal properties to individual AuNPs. Our results demonstrated enhanced photothermal properties through the dramatic increase in PNB generation, lifetime, and probability at significantly lower laser fluencies than individual AuNPs, which required 7 times the laser energy to generate PNBs. Furthermore, we computationally studied the thermal transport of QβAuNP scaffolds and compared them with the individual AuNPs and found that these scaffolds induce delocalized heating among AuNPs, leading to more rapid heating and more gradual heat dissipation compared to individual AuNPs, correlating well with superior PNB formation at lower laser fluences. These results provide a promising outlook that can significantly contribute to applications in biomedicine, photothermal cancer therapies, and therapeutic drug delivery systems.

Supplementary Material

Refer to Web version on PubMed Central for supplementary material.

ACKNOWLEDGMENTS

We thank Dr. Jon Pokorski for providing us with E. Coli BL21-CE3 cells. J.J.G acknowledges support from the National Science Foundation (DMR-2003534) and the Welch Foundation (AT-1989-20190330).

ABBREVIATIONS

AuNP	gold nanoparticles

QβAuNP	Qβ gold nanoparticles
PNB	plasmonic nanobubble
Cabs	cross-section absorption

REFERENCES

(1). Bayda S; Adeel M; Tuccinardi T; Cordani M; Rizzolio F The History of Nanoscience and Nanotechnology: From Chemical-Physical Applications to Nanomedicine. Molecules 2019, 25 (1). DOI: 10.3390/molecules25010112.

(2). Amendola V; Pilot R; Frasconi M; Marago OM; Iati MA Surface plasmon resonance in gold nanoparticles: a review. J Phys Condens Matter 2017, 29 (20), 203002. DOI: 10.1088/1361-648X/aa60f3. [PubMed: 28426435]

(3). Lashkari SM; Kariminezhad H; Safarnezhad N; Amani H Surface plasmon resonance of naked gold nanoparticles for photodynamic inactivation of Escherichia coli. Gold Bulletin 2019, 52 (1), 51–60. DOI: 10.1007/s13404-019-00252-2.

(4). Su Y-H; Ke Y-F; Cai S-L; Yao Q-Y Surface plasmon resonance of layer-by-layer gold nanoparticles induced photoelectric current in environmentally-friendly plasmon-sensitized solar cell. Light: Science & Applications 2012, 1 (6), e14–e14. DOI: 10.1038/lsa.2012.14.

(5). Li X; Kang P; Chen Z; Lal S; Zhang L; Gassensmith JJ; Qin Z Rock the nucleus: significantly enhanced nuclear membrane permeability and gene transfection by plasmonic nanobubble induced nanomechanical transduction. Chemical Communications 2018, 54 (20), 2479–2482, 10.1039/C7CC09613E. DOI: 10.1039/C7CC09613E. [PubMed: 29376174]

(6). Huang X; El-Sayed MA Gold nanoparticles: Optical properties and implementations in cancer diagnosis and photothermal therapy. Journal of Advanced Research 2010, 1 (1), 13–28. DOI: 10.1016/j.jare.2010.02.002.

(7). Kim HS; Lee DY Near-Infrared-Responsive Cancer Photothermal and Photodynamic Therapy Using Gold Nanoparticles. Polymers (Basel) 2018, 10 (9). DOI: 10.3390/polym10090961.

(8). Rozanova N; Zhang J Photothermal ablation therapy for cancer based on metal nanostructures. Science in China Series B: Chemistry 2009, 52 (10), 1559–1575. DOI: 10.1007/s11426-009-0247-0.

(9). Wagner DS; Delk NA; Lukianova-Hleb EY; Hafner JH; Farach-Carson MC; Lapotko DO The in vivo performance of plasmonic nanobubbles as cell theranostic agents in zebrafish hosting prostate cancer xenografts. Biomaterials 2010, 31 (29), 7567–7574. DOI: 10.1016/j.biomaterials.2010.06.031. [PubMed: 20630586]

(10). Kang P; Chen Z; Nielsen SO; Hoyt K; D'Arcy S; Gassensmith JJ; Qin Z Molecular Hyperthermia: Spatiotemporal Protein Unfolding and Inactivation by Nanosecond Plasmonic Heating. Small 2017, 13 (36), 1700841. DOI: 10.1002/smll.201700841.

(11). Qin Z; Bischof JC Thermophysical and biological responses of gold nanoparticle laser heating. Chem Soc Rev 2012, 41 (3), 1191–1217. DOI: 10.1039/c1cs15184c. [PubMed: 21947414]

(12). Li X; Vemireddy V; Cai Q; Xiong H; Kang P; Li X; Giannotta M; Hayenga HN; Pan E; Sirsi SR; et al. Reversibly Modulating the Blood-Brain Barrier by Laser Stimulation of Molecular-Targeted Nanoparticles. Nano Lett 2021, 21 (22), 9805–9815. DOI: 10.1021/acs.nanolett.1c02996. [PubMed: 34516144]

(13). Li X; Cai Q; Wilson BA; Fan H; Giannotta M; Bachoo R; Qin Z Calcium-Mediated Modulation of Blood-Brain Barrier Permeability by Laser Stimulation of Endothelial-Targeted Nanoparticles. bioRxiv 2022, 2022.2006.2002.494541. DOI: 10.1101/2022.06.02.494541.

(14). Bromley KM; Patil AJ; Perriman AW; Stubbs G; Mann S Preparation of high quality nanowires by tobacco mosaic virus templating of gold nanoparticles. Journal of Materials Chemistry 2008, 18 (40). DOI: 10.1039/b809585j.

(15). Fernandes R; Li M; Dujardin E; Mann S; Kanaras AG Ligand-mediated self-assembly of polymer-enveloped gold nanoparticle chains and networks. Chemical communications 2010, 46 (40), 7602–7604. [PubMed: 20835475]

(16). Mann S Self-assembly and transformation of hybrid nano-objects and nanostructures under equilibrium and non-equilibrium conditions. Nature materials 2009, 8 (10), 781–792. [PubMed: 19734883]

(17). Shenton W; Davis SA; Mann S Directed Self-Assembly of Nanoparticles into Macroscopic Materials Using Antibody – Antigen Recognition. Advanced Materials 1999, 11 (6), 449–452.

(18). Zhou K; Zhang J; Wang Q Site-selective nucleation and controlled growth of gold nanostructures in tobacco mosaic virus nanotubulars. Small 2015, 11 (21), 2505–2509. [PubMed: 25612918]

(19). Li F; Wang Q Fabrication of nanoarchitectures templated by virus-based nanoparticles: strategies and applications. Small 2014, 10 (2), 230–245. [PubMed: 23996911]

(20). Lukianova-Hleb E; Hu Y; Latterini L; Tarpani L; Lee S; Drezek RA; Hafner JH; Lapotko DO Plasmonic Nanobubbles as Transient Vapor Nanobubbles Generated around Plasmonic Nanoparticles. ACS Nano 2010, 4 (4), 2109–2123. DOI: 10.1021/nn1000222. [PubMed: 20307085]

(21). Lukianova-Hleb EY; Hanna EY; Hafner JH; Lapotko DO Tunable plasmonic nanobubbles for cell theranostics. Nanotechnology 2010, 21 (8), 085102. DOI: 10.1088/0957-4484/21/8/085102.

(22). Lukianova-Hleb EY; Kim Y-S; Belatsarkouski I; Gillenwater AM; O'Neill BE; Lapotko DO Intraoperative diagnostics and elimination of residual microtumours with plasmonic nanobubbles. Nature Nanotechnology 2016, 11 (6), 525–532. DOI: 10.1038/nnano.2015.343.

(23). Lukianova-Hleb EY; Koneva II; Oginsky AO; La Francesca S; Lapotko DO Selective and self-guided micro-ablation of tissue with plasmonic nanobubbles. J Surg Res 2011, 166 (1), e3–13. DOI: 10.1016/j.jss.2010.10.039. [PubMed: 21176913]

(24). Lukianova-Hleb EY; Ren X; Sawant RR; Wu X; Torchilin VP; Lapotko DO On-demand intracellular amplification of chemoradiation with cancer-specific plasmonic nanobubbles. Nature Medicine 2014, 20 (7), 778–784. DOI: 10.1038/nm.3484.

(25). Lukianova-Hleb EY; Ren X; Townley D; Wu X; Kupferman ME; Lapotko DO Plasmonic nanobubbles rapidly detect and destroy drug-resistant tumors. Theranostics 2012, 2 (10), 976–987. DOI: 10.7150/thno.5116. [PubMed: 23139725]

(26). Lukianova-Hleb EY; Volkov AN; Lapotko DO Laser Pulse Duration Is Critical For the Generation of Plasmonic Nanobubbles. Langmuir 2014, 30 (25), 7425–7434. DOI: 10.1021/la5015362. [PubMed: 24916057]

(27). Kitz M; Preisser S; Wetterwald A; Jaeger M; Thalmann GN; Frenz M Vapor bubble generation around gold nano-particles and its application to damaging of cells. Biomed. Opt. Express 2011, 2 (2), 291–304. DOI: 10.1364/BOE.2.000291. [PubMed: 21339875]

(28). Danysh BP; Constantinou PE; Lukianova-Hleb EY; Lapotko DO; Carson DD The MUC1 Ectodomain: A Novel and Efficient Target for Gold Nanoparticle Clustering and Vapor Nanobubble Generation. Theranostics 2012, 2 (8), 777–787. DOI: 10.7150/thno.4494 From NLM. [PubMed: 22916077]

(29). Lukianova-Hleb EY; Ren X; Zasadzinski JA; Wu X; Lapotko DO Plasmonic nanobubbles enhance efficacy and selectivity of chemotherapy against drug-resistant cancer cells. Adv Mater 2012, 24 (28), 3831–3837. DOI: 10.1002/adma.201103550 From NLM. [PubMed: 22407874]

(30). Shahrivarkevishahi A; Hagge LM; Brohlin OR; Kumari S; Ehrman R; Benjamin C; Gassensmith JJ Virus-like particles: a self-assembled toolbox for cancer therapy. Materials Today Chemistry 2022, 24, 100808. DOI: 10.1016/j.mtchem.2022.100808.

(31). Chen Z; Li N; Li S; Dharmarwardana M; Schlimme A; Gassensmith JJ Viral chemistry: the chemical functionalization of viral architectures to create new technology. Wiley Interdiscip Rev Nanomed Nanobiotechnol 2016, 8 (4), 512–534. DOI: 10.1002/wnan.1379. [PubMed: 26663821]

(32). Rohovie MJ; Nagasawa M; Swartz JR Virus-like particles: Next-generation nanoparticles for targeted therapeutic delivery. Bioeng Transl Med 2017, 2 (1), 43–57. DOI: 10.1002/btm2.10049. [PubMed: 29313023]

(33). Lumata JL; Ball D; Shahrivarkevishahi A; Luzuriaga MA; Herbert FC; Brohlin O; Lee H; Hagge LM; D'Arcy S; Gassensmith JJ Identification and physical characterization of a spontaneous mutation of the tobacco mosaic virus in the laboratory environment. Sci Rep 2021, 11 (1), 15109. DOI: 10.1038/s41598-021-94561-2. [PubMed: 34302022]

(34). Li S; Gassensmith JJ Synthesis of Metal-Organic Frameworks on Tobacco Mosaic Virus Templates. Methods Mol Biol 2018, 1798, 95–108. DOI: 10.1007/978-1-4939-7893-9_8. [PubMed: 29868954]

(35). Luzuriaga MA; Welch RP; Dharmarwardana M; Benjamin CE; Li S; Shahrivarkevishahi A; Popal S; Tuong LH; Creswell CT; Gassensmith JJ Enhanced Stability and Controlled Delivery of MOF-Encapsulated Vaccines and Their Immunogenic Response In Vivo. ACS Appl Mater Interfaces 2019, 11 (10), 9740–9746. DOI: 10.1021/acsami.8b20504. [PubMed: 30776885]

(36). Herbert FC; Brohlin OR; Galbraith T; Benjamin C; Reyes CA; Luzuriaga MA; Shahrivarkevishahi A; Gassensmith JJ Supramolecular Encapsulation of Small-Ultrared Fluorescent Proteins in Virus-Like Nanoparticles for Noninvasive In Vivo Imaging Agents. Bioconjug Chem 2020, 31 (5), 1529–1536. DOI: 10.1021/acs.bioconjchem.0c00190. [PubMed: 32343135]

(37). Shahrivarkevishahi A; Luzuriaga MA; Herbert FC; Tumac AC; Brohlin OR; Wijesundara YH; Adlooru AV; Benjamin C; Lee H; Parsamian P; et al. PhotothermalPhage: A Virus-Based Photothermal Therapeutic Agent. J Am Chem Soc 2021, 143 (40), 16428–16438. DOI: 10.1021/jacs.1c05090. [PubMed: 34551259]

(38). Benjamin CE; Chen Z; Kang P; Wilson BA; Li N; Nielsen SO; Qin Z; Gassensmith JJ Site-Selective Nucleation and Size Control of Gold Nanoparticle Photothermal Antennae on the Pore Structures of a Virus. J Am Chem Soc 2018, 140 (49), 17226–17233. DOI: 10.1021/jacs.8b10446. [PubMed: 30452248]

(39). Golmohammadi R; Fridborg K; Bundule M; Valegård K; Liljas L The crystal structure of bacteriophage Qβ at 3.5 å resolution. Structure 1996, 4 (5), 543–554. DOI: 10.1016/S0969-2126(96)00060-3. [PubMed: 8736553]

(40). Banerjee D; Liu AP; Voss NR; Schmid SL; Finn MG Multivalent display and receptor-mediated endocytosis of transferrin on virus-like particles. Chembiochem 2010, 11 (9), 1273–1279. DOI: 10.1002/cbic.201000125 PubMed. [PubMed: 20455239]

(41). Rhee J-K; Hovlid M; Fiedler JD; Brown SD; Manzenrieder F; Kitagishi H; Nycholat C; Paulson JC; Finn MG Colorful virus-like particles: fluorescent protein packaging by the Qβ capsid. Biomacromolecules 2011, 12 (11), 3977–3981. DOI: 10.1021/bm200983k PubMed. [PubMed: 21995513]

(42). Pokorski JK; Hovlid ML; Finn MG Cell Targeting with Hybrid Qβ Virus-Like Particles Displaying Epidermal Growth Factor. Chembiochem 2011, 12 (16), 2441–2447. DOI: 10.1002/cbic.201100469. [PubMed: 21956837]

(43). Chen Z; Boyd SD; Calvo JS; Murray KW; Mejia GL; Benjamin CE; Welch RP; Winkler DD; Meloni G; D'Arcy S; et al. Fluorescent Functionalization across Quaternary Structure in a Virus-like Particle. Bioconjugate Chemistry 2017, 28 (9), 2277–2283. DOI: 10.1021/acs.bioconjchem.7b00305. [PubMed: 28787574]

(44). Lee H; Benjamin CE; Nowak CM; Tuong LH; Welch RP; Chen Z; Dharmarwardana M; Murray KW; Bleris L; D'Arcy S; et al. Regulating the Uptake of Viral Nanoparticles in Macrophage and Cancer Cells via a pH Switch. Molecular Pharmaceutics 2018, 15 (8), 2984–2990. DOI: 10.1021/acs.molpharmaceut.8b00348. [PubMed: 29787282]

(45). Benjamin CE; Chen Z; Brohlin OR; Lee H; Shahrivarkevishahi A; Boyd S; Winkler DD; Gassensmith JJ Using FRET to measure the time it takes for a cell to destroy a virus. Nanoscale 2020, 12 (16), 9124–9132. DOI: 10.1039/c9nr09816j. [PubMed: 32292962]

(46). Benjamin C; Brohlin O; Shahrivarkevishahi A; Gassensmith JJ Chapter 11 - Virus like particles: fundamental concepts, biological interactions, and clinical applications. In Nanoparticles for Biomedical Applications, Chung EJ, Leon L, Rinaldi C Eds.; Elsevier, 2020; pp 153–174.

(47). Lee H; Shahrivarkevishahi A; Lumata JL; Luzuriaga MA; Hagge LM; Benjamin CE; Brohlin OR; Parish CR; Firouzi HR; Nielsen SO; et al. Supramolecular and biomacromolecular enhancement of metal-free magnetic resonance imaging contrast agents. Chemical Science 2020, 11 (8), 2045–2050, 10.1039/C9SC05510J. DOI: 10.1039/C9SC05510J. [PubMed: 32180926]

(48). Wijesundara YH; Herbert FC; Kumari S; Howlett T; Koirala S; Trashi O; Trashi I; Al-Kharji NM; Gassensmith JJ Rip it, stitch it, click it: A Chemist's guide to VLP manipulation. Virology 2022, 577, 105–123. DOI: 10.1016/j.virol.2022.10.008. [PubMed: 36343470]

(49). Xie C; Qin Z Spatiotemporal Evolution of Temperature During Transient Heating of Nanoparticle Arrays. Journal of heat transfer 2021, 144 3, 031204.

(50). Ogunyankin MO; Shin JE; Lapotko DO; Ferry VE; Zasadzinski JA Optimizing the NIR Fluence Threshold for Nanobubble Generation by Controlled Synthesis of 10–40 nm Hollow Gold Nanoshells. Advanced Functional Materials 2018, 28 (10), 1705272. DOI: 10.1002/adfm.201705272. [PubMed: 31467502]

(51). Vines JB; Yoon J-H; Ryu N-E; Lim D-J; Park H Gold Nanoparticles for Photothermal Cancer Therapy. Frontiers in chemistry 2019, 7, 167–167. DOI: 10.3389/fchem.2019.00167. [PubMed: 31024882]

(52). Kennedy LC; Bickford LR; Lewinski NA; Coughlin AJ; Hu Y; Day ES; West JL; Drezek RA A New Era for Cancer Treatment: Gold-Nanoparticle-Mediated Thermal Therapies. Small (Weinheim an der Bergstrasse, Germany) 2011, 7 (2), 169–183. DOI: 10.1002/smll.201000134. [PubMed: 21213377]

(53). Xie C; Qin Z Spatiotemporal Evolution of Temperature During Transient Heating of Nanoparticle Arrays. Journal of Heat Transfer 2022, 144 (3). DOI: 10.1115/1.4053196 (acccessed 7/5/2022).

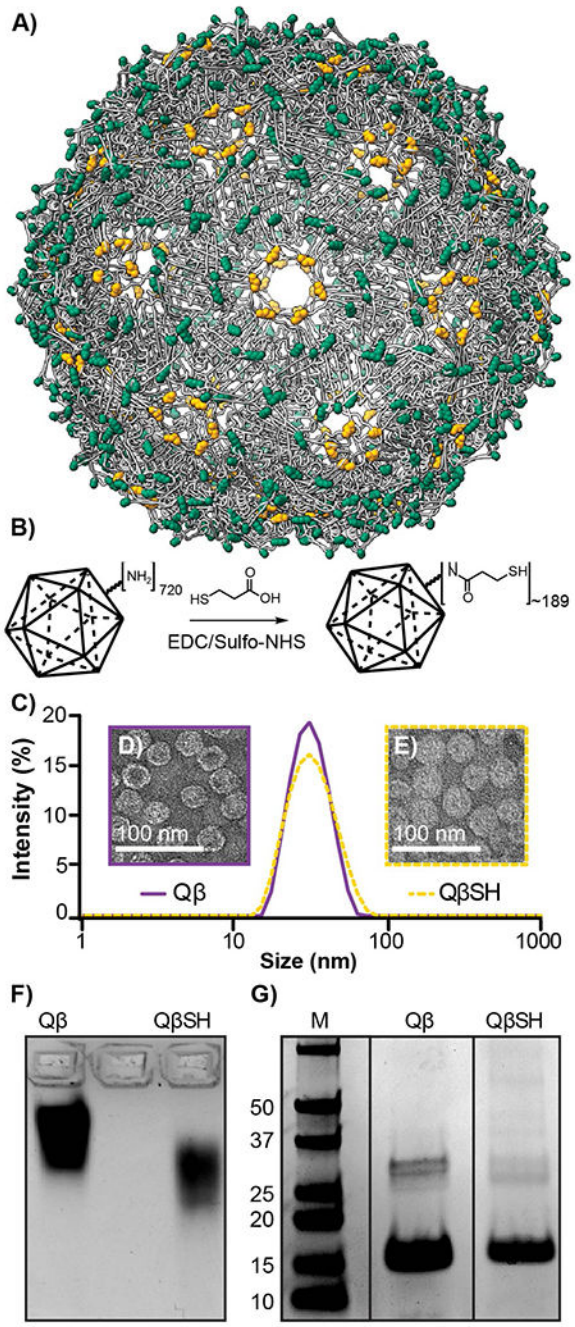

Figure 1.

A) Qβ, an icosahedral virus-like particle (VLP), is composed of 180 coat proteins connected through disulfide bonds (yellow). In addition, each coat protein has four solvent-exposed primary amine residues (green) available for bioconjugation. **B)** A scheme illustrating Qβ surface functionalization of 3-mercaptopropionic acid (MPA) through EDC/sulfo-NHS coupling. **C)** DLS of Qβ (purple) and QβSH (yellow-dashed). **D)** TEM of Qβ (purple) and **E)** QβSH (yellow-dashed). **F)** Coomassie-stained 1% agarose gel of Qβ (left) and QβSH (Right) and **G)** SDS-PAGE gel of Qβ (left) and QβSH (Right).

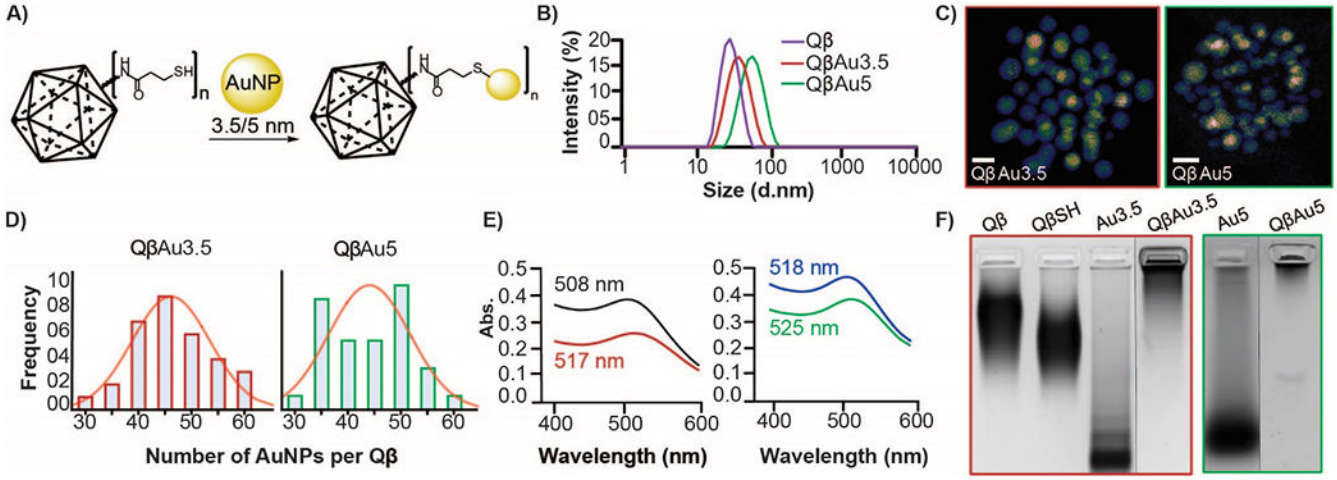

Figure 2.

A) A scheme illustrating 3.5 and 5 nm AuNPs immobilization onto the surface of QβSH. **B)** DLS of Qβ and QβAuNPs. **C)** STEM micrographs of immobilized AuNPs onto the surface of QβSH. Scale bar: 5 nm **D)** Distribution frequency of immobilized AuNPs to functionalized Qβ thiol: Au3.5 (left) and Au5 (Right) (n=32 per size). **E)** UV-Vis spectra show a redshift of Au3.5 (black) and Au5 (blue) to immobilized QβAuNPs (QβAu3.5 (red) and QβAu5 (green)). **F)** Coomassie-stained 1% agarose gel of Qβ, QβSH, AuNPs, and QβAuNPs.

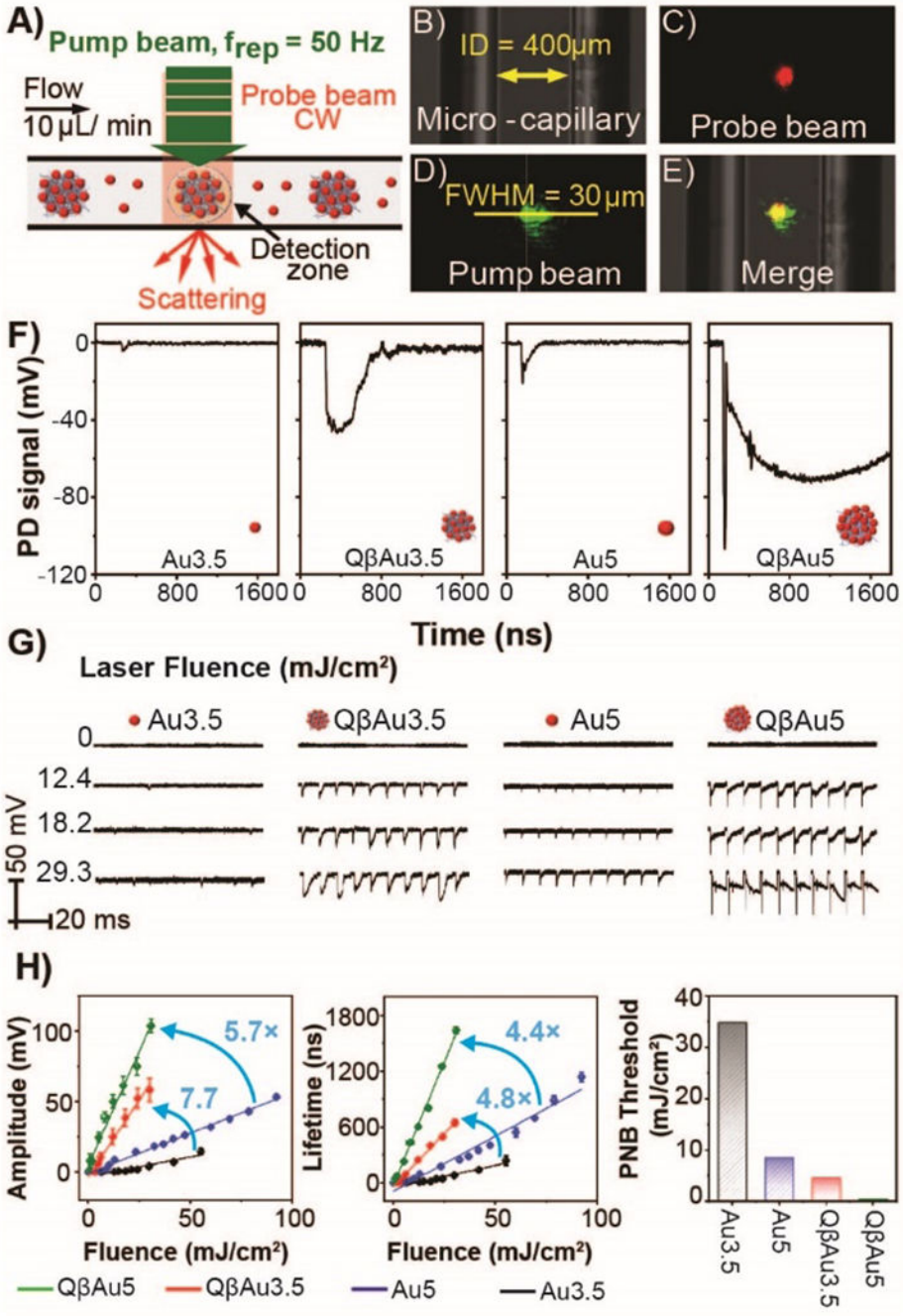

Figure 3. Plasmonic Nanobubble detection for individual AuNPs and conjugated QβAuNPs.

A) Schematic illustration of PNB detection. **B)** Bright-field images of 400 µm borosilicate glass microcapillary, **C)** 633 nm probe laser beam, **D)** 532 nm pump laser beam, where the beam diameter is calculated based on the full width half maximum (FWHM) of the intensity profile of the Gaussian pump beam, and **E)** two aligned laser beams merged inside the microcapillary. **F)** Typical PNB signals generated by Au3.5, QβAu3.5, Au5, and QβAu5 with the same optical density (O.D.=0.4) at the laser fluence = 29.3 mJ/cm^2. **G)** Representative PNB signal traces (10 pulses) collected for samples from Au3.5, QβAu3.5,

Au5, and QβAu5, respectively. PNB signals analysis by **(H)** amplitude, **(I)** lifetime, and **(J)** energy threshold was plotted for small AuNPs and conjugated QβAuNPs upon different laser fluence heating.

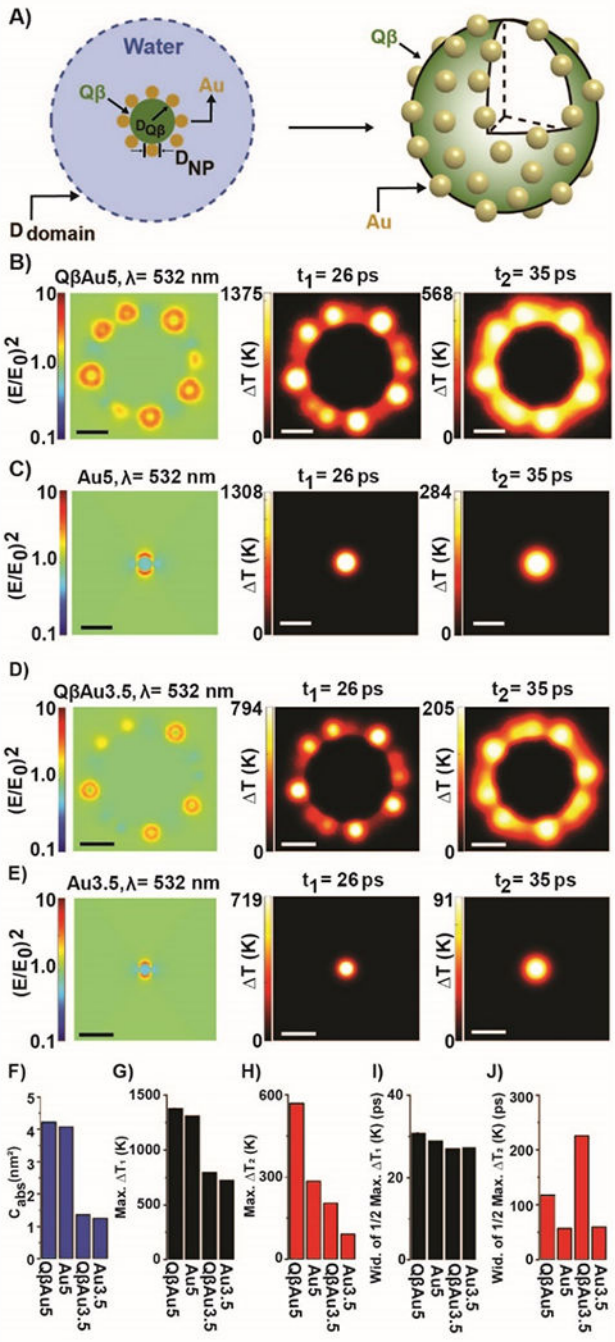

Figure 4. Temperature rise (Δ*T*) during the transient heating of individual AuNPs and conjugated QβAuNPs.

A) Schematic illustration of the model. The AuNPs are distributed in a Fibonacci lattice on the surface of the Qβ capsid, and the QβAuNPs are submerged in water. **B-E)** Near field enhancement ($(E/E_0)^2$) profile and temperature rise (Δ*T*) profile for QβAu5, Au5, QβAu3.5, and Au3.5. The scale bar represents 10 nm. The comparison of **F)** C_{abs}, **G)** maximum of ΔT_1, **H)** maximum of ΔT_2, **I)** The width of half maximum ΔT_1, **J)** The width of half

maximum ΔT_2 for QβAu5, Au5, QβAu3.5, and Au3.5. Laser fluence for all cases is 34.8 mJ/cm^2.

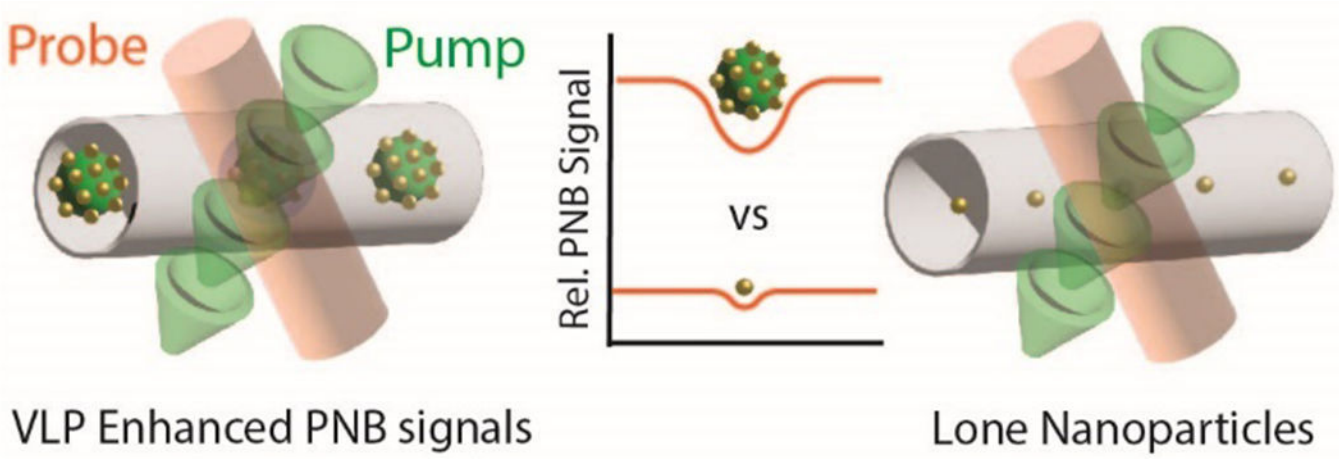

Scheme 1.

A schematic illustration of plasmonic nanobubble signal generation comparing sub-10 nm AuNPs immobilized onto VLP scaffolds vs. individual sub-10 nm AuNPs.